Supplemental Material: Giant 2D Skyrmion Topological Hall Effect with Ultrawide Temperature Window and Low-Current Manipulation in 2D Room-Temperature Ferromagnetic Crystals

Gaojie Zhang(张高节),[1, 2] Qingyuan Luo(罗清源),[3] Xiaokun Wen(文晓琨),[1, 2] Hao Wu(武浩),[1, 2, *] Li Yang(杨丽),[1, 2] Wen Jin(靳雯),[1, 2] Luji Li(李路吉),[1, 2] Jia Zhang(张佳),[4] Wenfeng Zhang(张文峰),[1, 2, 5] Haibo Shu(舒海波),[3, *] and Haixin Chang(常海欣)[1, 2, 5, *]

[1]*State Key Laboratory of Material Processing and Die & Mold Technology, School of Materials Science and Engineering, Huazhong University of Science and Technology, Wuhan 430074, China*

[2]*Wuhan National High Magnetic Field Center and Institute for Quantum Science and Engineering, Huazhong University of Science and Technology, Wuhan 430074, China*

[3]*College of Optical and Electronic Technology, China Jiliang University, Hangzhou 310018, China*

[4]*School of Physics and Wuhan National High Magnetic Field Center, Huazhong University of Science and Technology, 430074 Wuhan, China.*

[5]*Shenzhen R&D Center of Huazhong University of Science and Technology, Shenzhen 518000, China*

This file includes:

Notes S1-S5:

Figures S1-S19:

nanosheets by EPMA.

Figure S4. XPS analysis on an O-FGaT/FGaT surface under different etching time.

Figure S5. Above-room-temperature strong ferromagnetism in pristine vdW bulk Fe_3GaTe_{2-x} crystals.

Figure S6. Magneto-transport measurement of a non-oxidized pristine 14 nm Fe_3GaTe_{2-x} nanosheet.

Figure S7. AFM images and the corresponded profile height of six as-tested Hall devices based on 2D O-FGaT/FGaT heterostructures.

Figure S8. Magneto-transport measurement of a 13 nm 2D O-FGaT/FGaT heterostructure.

Figure S9. Natural total oxidation of the 2D Fe_3GaTe_{2-x} nanosheets in the air for 48 h.

Figure S10. Observation of Néel-type skyrmions in 2D O-FGaT/FGaT by Lorentz-TEM with the perpendicular magnetic field at 300 K.

Figure S11. Magnetic-field-driven evolution from stripe domains to skyrmions in a thin 2D O-FGaT/FGaT by Lorentz-TEM with perpendicular magnetic field at 300 K.

Figure S12. Lorentz-TEM images under different perpendicular magnetic field in a pristine non-oxidized thin 2D Fe_3GaTe_{2-x} nanosheet at 300 K under α=29°, d=-2 mm.

Figure S13. Extracting the THE signals in 2D O-FGaT/FGaT by step function.

Figure S14. Temperature-dependent ρ_{TH}-B curves for two 2D O-FGaT/FGaT heterostructures with different thickness.

Figure S15. Magnetic field dependence of the skyrmion density and ρ_{TH} at room temperature in 2D O-FGaT/FGaT.

Figure S16. Comparison of THE tests-derived minimum skyrmion size ($n_{sk}^{-1/2}$) in various 2D skyrmion systems.

Figure S17. ρ_{xx} and saturated ρ_{AH} as a function of current densities in 2D O-FGaT/FGaT at room temperature.

Figure S18. Theoretical model for calculating DMI in Fe_3GaTe_{2-x}.

Figure S19. The density of states (DOSs) comparison of total, Fe-3d, Ga-4p, and Te-5p in oxidized bilayer Fe_3GaTe_{2-x} with that of pristine bilayer Fe_3GaTe_{2-x}.

Tables S1-S5:

Table S1. Magneto-transport parameters for THE calculation in 2D O-FGaT/FGaT heterostructures with different thickness.

Table S2. Comparison of the THE temperature window and maximum ρ_{TH} in various 2D skyrmion systems from the literatures.

Table S3. Comparison of critical current density (j_c) and maximum drift velocity (v_d) in various room-temperature 2D skyrmion systems from literatures.

Table S4. The binding energies (E_b) for incorporating oxygen into Fe_3GaTe_{2-x} and Fe_3GaTe_2 crystals.

Table S5. Average Bader charges (Q) of single atom in pristine, O-substituted, and O-interstitial bilayer Fe_3GaTe_{2-x}.

Note S1. XPS results under different etching time for surface oxidation analysis

In the initial state without etching, the Fe 2p spectra is decomposed into Fe $2p_{3/2}$ and Fe $2p_{1/2}$ (**Figure S4a**). Specifically, two peaks at 706.7 and 719. 8 eV come from the Fe(0). The other two peaks at 710.8 and 724.4 eV are ascribed to the Fe(III). Meanwhile, the Ga 2p spectra is decomposed into Ga $2p_{3/2}$ and Ga $2p_{1/2}$ peaks with binding energies of 1117.8 and 1144.7 eV, corresponding to the

natively-oxidized Ga(II) (**Figure S4b**). And then, the Te spectra can be decomposed into Te $3d_{5/2}$ and Te $3d_{3/2}$. Two peaks at 572.8 and 583.2 eV correspond to the Te (II). Other four peaks at 576.3, 586.7, 573.9, and 584.4 eV all originate from the oxidized Te (**Figure S4c**). Moreover, the O 1s spectra are decomposed into three peaks including 530.5, 531.6, and 532.9 eV, corresponding to the substitutional oxygen, interstitial oxygen and adsorbed oxygen, respectively (**Figure S4d**)[1].

With the increase of etching time, the oxidation peaks of Te 3d gradually decrease and eventually disappear. At the same time, note that the emergence of Fe(II), Ga(II) peaks and the increase of Fe(0), Fe(II), Ga(II) peaks are attributed to the reduction effect of Ar^+ during the etching process, which can also be seen in other reports[2,3]. Together with cross-sectional TEM imaging and elemental mapping, all these results indicate the presence of an ultrathin O-FGaT layer on the surface of the Fe_3GaTe_{2-x} crystal.

Note S2. Strong intrinsic ferromagnetism in the bulk Fe_3GaTe_{2-x} crystal and 2D Fe_3GaTe_{2-x} nanosheet

The temperature dependent magnetization (M-T) curves under zero-field-cooling and field-cooling (ZFC-FC) regime of bulk Fe_3GaTe_{2-x} crystal exhibit a typically ferromagnetic feature and an above-room-temperature T_C (~358 K) (**Figure S5a,b**), higher than most known 2D vdW ferromagnets[4-7]. Moreover, the magnetization of out-of-plane ZFC-FC curve is larger than that of in-plane ZFC-FC curve, demonstrating the PMA in bulk Fe_3GaTe_{2-x} crystal. A same conclusion can also be obtained from the out-of-plane and in-plane magnetized M-B curves with significantly different shapes (**Figure S5c,d**). The PMA energy density (K_u) is determined by the following formula[8]:

$$K_u = \frac{B_{sat} M_{sat}}{2} \quad (1)$$

where B_{sat} is the saturation field of hard axis, M_{sat} is the saturation magnetization. Among them, the B_{sat} of bulk Fe_3GaTe_{2-x} crystal is determined by VSM test under 300 K and in-plane magnetic field from -9 to 9 T (**Figure S5e**). The M_{sat} and H_C of bulk Fe_3GaTe_{2-x} crystal are measured by VSM tests under different temperatures (**Figure S5f**). Therefore, the K_u of bulk Fe_3GaTe_{2-x} crystal is calculated as ~4.65×10^5 J/m^3 at 300 K, consistent with the previous report[9]. Such large room-temperature K_u is one order of magnitude larger than known vdW ferromagnets (*e.g.* $CrTe_2$[10]) and is better than non-vdW ferromagnetic films (*e.g.* CoFeB[8]). The bulk Fe_3GaTe_{2-x} crystal is a hard ferromagnet at 10 K (H_C, ~830 Oe) and turn into a soft ferromagnet at 300 K (H_C, ~200 Oe). In addition, the M_{sat} of bulk Fe_3GaTe_{2-x} crystal is ~55.1 emu/g at 10 K and remain ~36.3 emu/g at 300 K, ~2.9 times that in 2D vdW ferromagnet $CrTe_2$ at room temperature[7].

To further study the 2D ferromagnetism, the magneto-transport measurement is performed on a non-oxidized 14 nm Fe_3GaTe_{2-x} nanosheet (**Figure S6a**). The typical metallic characteristic is observed from the temperature-dependent longitudinal resistivity (ρ_{xx}-T) curve, where the ρ_{xx} (300 K)=3.24×10^2 μΩ·cm (**Figure S6b**). As shown in **Figure S6c**, the AHE exists when the temperature is below T_C ~350 K and the square hysteresis loop with nearly vertical magnetization flipping persists at ~320 K, demonstrating the coexistence of long-range ferromagnetism and large PMA at above room temperature in 2D Fe_3GaTe_{2-x} nanosheet. Compared with 2D O-FGaT/FGaT heterostructures, the 14 nm Fe_3GaTe_{2-x} nanosheet shows no THE in the ρ_{xy}-B curves at all temperatures. Further, we carefully record the ρ_{AH} and H_C as a function of temperature, thereby

implying the influence of thermal fluctuation on 2D ferromagnetism (**Figure S6d,e**). Unlike H_C, which decreases with increasing temperature, the ρ_{AH} is almost constant at first, and then gradually decreases after the temperature exceeds 150 K.

Note S3. Discussion of excluding the artifact "THE" signals

Recent criticisms about some THE may come from the artificial multiple conduction channels, since most hump and dip features can indeed be superposed by two-component AHE with opposite signs and different H_C[11-15]. Identifying this concern requires understanding the rationale behind it. An artifact "THE" mainly happens in heterostructures with parallel multi-conduction channels, or in inhomogeneous ferromagnets[16]. Fortunately, Seung-Hyun Chun et al.[17] and Kang L. Wang et al.[18] reported some guidance methods for distinguishing the artifact "THE" and real THE.

For the concern of parallel multi-conduction channels, one example is a $(Bi, Sb)_2Te_3/(V, Bi, Sb)_2Te_3$ heterostructure which contains both surface and bulk ferromagnetism, forming two-component AHE with opposite signs and different H_C[12]. To discuss this case, we let a 2D Fe_3GaTe_{2-x} nanosheet oxidize naturally in the air for 48 h and record the change of ρ_{xx} at 300 K (**Figure S9a**). Note that oxidation for 48 h is sufficient to completely oxidize this Fe_3GaTe_{2-x} nanosheet, forming an ~8 nm O-FGaT layer confirmed by AFM and cross-sectional TEM (**Figure S9b,c**). The room-temperature ρ_{xx} of this 8 nm O-FGaT layer reaches to 1.23×10^7 μΩ·cm, which is ~10^5 times that in non-oxidized 2D Fe_3GaTe_{2-x} nanosheet (**Figure S6b**). Therefore, we believe that the current totally flow in the Fe_3GaTe_{2-x}, as the resistivity of O-FGaT layer is too large to contribute to the conduction. A similar method of excluding artifact "THE" has been endorsed in another report[17].

For the concern of inhomogeneous ferromagnets, a ferromagnet with inhomogeneous thickness (*e.g.* $SrRuO_3$[14,15]) or containing hidden ferromagnetic phase (*e.g.* $MnBi_2Te_4$ films containing $MnTe_2$[18]) sometimes leads to two spatially separated ferromagnetic regions and present two-component AHE with opposite signs and different H_C[13]. The difference in the temperature dependence of such two-component AHE results in the polarity change of the total AHE in a narrow temperature range, where an artifact "THE" occurs[11,14]. In contrast, temperature-dependent real THE with AHE reveals no such polarity change of AHE, as real THE only occurs around the spin-flipping region of the AHE and should not affect the polarity of the AHE[18]. In this work, no temperature- or thickness-induced polarity change of AHE are observed in all 2D O-FGaT/FGaT heterostructures (**main text Figure 2d,e** and **Figure S8c**), and robust 2D THE exists in a wide temperature window ranging from 2 to 300 K (**main text Figure 3e**). Also, as a controlled sample, the non-oxidized 14 nm Fe_3GaTe_{2-x} nanosheet shows neither the temperature-induced polarity change of AHE nor the THE (**Figure S6c**), and the selected-area electron diffraction (SAED) result for non-oxidized Fe_3GaTe_{2-x} shows a set of clean diffraction spots for single crystals without hidden ferromagnetic phase (**Figure S2b**). Therefore, we believe that the 2D THE in this work is induced by magnetic skyrmions rather than a superposition of multiple AHE.

Note S4. Additional analysis of THE and resulted THE-derived skyrmion sizes

For ferromagnetic materials with skyrmion lattice, the Hall resistivity (ρ_{xy}) can be decomposed into ρ_{OH}, ρ_{AH} and ρ_{TH}, which is further expressed by the following formula[19]:

$$\rho_{xy}=R_0\mu_0H+R_sM+\rho_{TH} \quad (2)$$

where R_0 is the ordinary Hall coefficient, R_s the anomalous Hall coefficient, M the magnetization, and ρ_{TH} the topological Hall resistivity.

Further, the ρ_{TH} induced by static skyrmions can be evaluated by the following formula[19]:

$$\rho_{TH}=PR_0B_{eff}=PR_0n_{sk}\emptyset_0 \quad (3)$$

where P is the spin polarization of carriers, R_0 the ordinary Hall coefficient, B_{eff} an effective magnetic field generated by the skyrmions, n_{sk} the 2D skyrmion density (assuming uniform, regular 2D skyrmion lattices, and each skyrmion carries a topological charge |Q|=1), and $\emptyset_0$ magnetic flux quantum ($\emptyset_0$=h/e, where h is the Plank constant and e is the electronic charge). To extract the R_0, the effect of ρ_{xx} on the ρ_{xy} is eliminated by the antisymmetric procedure:

$$\rho_+'(H)=[\rho_+(H)-\rho_-(-H)]/2 \quad (4)$$

$$\rho_-'(H)=[\rho_-(H)-\rho_+(-H)]/2 \quad (5)$$

Since the value of P have been recently calculated to be 67% at 10 K and 55% at 300 K in 2D Fe_3GaTe_2-based magnetic tunneling junctions[20], the single skyrmion size ($n_{sk}^{-1/2}$) of each 2D O-FGaT/FGaT heterostructure can be roughly derived (**Table S1**) if we reasonably suppose 2D Fe_3GaTe_{2-x} has similar spin polarization with Fe_3GaTe_2 since they have similar ferromagnetic properties as shown above.

Note S5. Discussion of Joule heating effect in current-controlled THE at room temperature

Before we study the current-dependent THE, the Joule heating effect should be discussed and excluded, as the increase of temperature may also influence the THE. In this work, we perform the current-controlled THE in 13 and 19 nm O-FGaT/FGaT heterostructures and evaluate the Joule heating effect by recording the longitudinal resistivity (ρ_{xx}) and saturated anomalous Hall resistivity (ρ_{AH}) at each current density. This evaluation method has also been applied to current tunable THE in other 2D skyrmion systems[21,22]. As we all know, the Joule heating effect will gradually increase with the increase of current density. Therefore, if the Joule heating effect is dominant, as the current density increases, the ρ_{xx} will increase while the saturated ρ_{AH} will decrease, similar to the metallic nature and temperature-dependent AHE, respectively. However, as shown in **Figure S17**, the fluctuation of ρ_{xx} and saturated ρ_{AH} with the increase of current densities are negligible, implying the negligible effect of Joule heating effect on the current-controlled THE tests. Furthermore, the relationship of j vs ρ_{TH} and j vs v_d in **main text Figure 4c,d** are consistent with the general magneto-transport law of skyrmion motion according to the previous report[22]. Thus, we believe the reduction of ρ_{TH} in this work may attribute to the current-driven skyrmion motion.

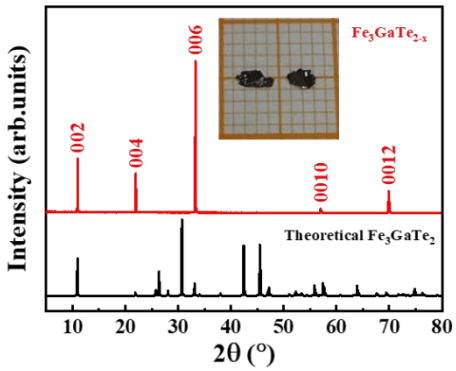

Figure S1. Crystal photograph and XRD pattern of the bulk Fe_3GaTe_{2-x} crystals. The size of each square in inset are 1×1 mm.

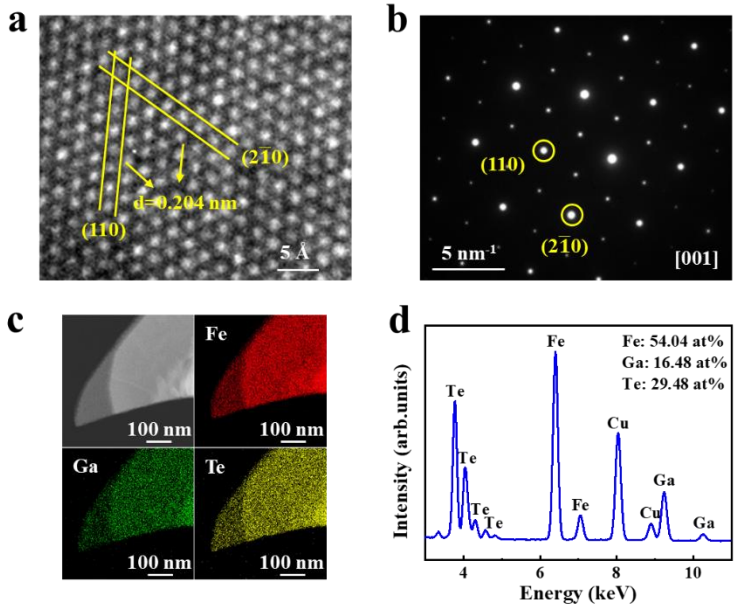

Figure S2. TEM characterization of a 2D Fe_3GaTe_{2-x} nanosheet along the [001] direction. (**a,b**) HRTEM image and corresponded SAED pattern of a Fe_3GaTe_{2-x} nanosheet. (**c,d**) EDS elemental mapping images and corresponded EDS spectrum of Fe, Ga, Te.

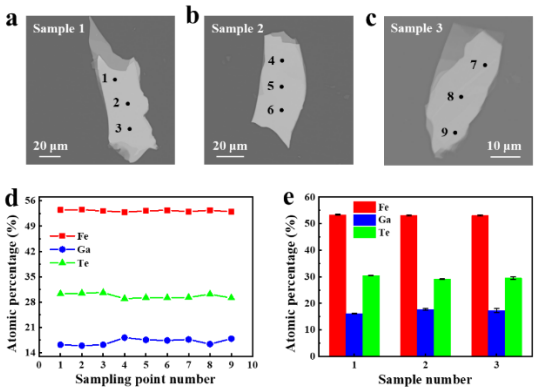

Figure S3. Quantitative analysis of Fe, Ga and Te content in three pristine Fe_3GaTe_{2-x} single-sheet nanosheets by EPMA. (**a-c**) EPMA images of three as-tested Fe_3GaTe_{2-x} nanosheets on SiO_2/Si substrate. The black points are sampling point. (**d**) Atomic percentages of Fe, Ga, and Te for each sampling point. (**e**) Average atomic percentages of Fe, Ga, and Te for sample 1 (Fe:Ga:Te=3.09:0.93:1.76), sample 2 (Fe:Ga:Te=3.11:1.04:1.70), and sample 3 (Fe:Ga:Te=3.11:1.01:1.73). Error bars s.d., N=3. These results demonstrate the existence of ~15 at% Te vacancies in the Fe_3GaTe_{2-x} crystal. Notably, before the formal EPMA test, Fe-contained, Ga-contained and Te-contained standard samples are used for calibration. For each Fe_3GaTe_{2-x} nanosheet, three positions are randomly selected and each is tested once.

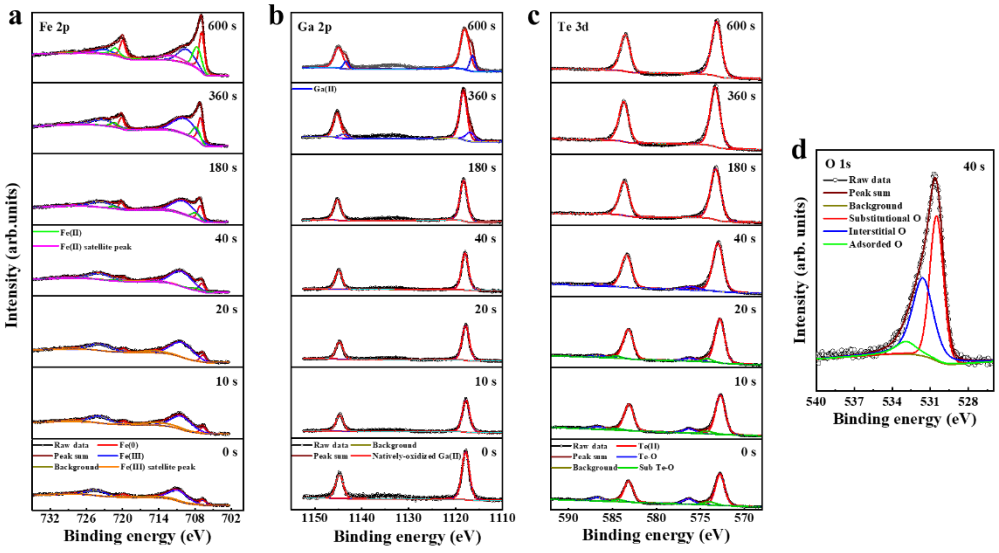

Figure S4. XPS analysis on an O-FGaT/FGaT surface under different etching time. (**a**) Fe 2p, (**b**) Ga 2p and (**c**) Te 3d. In order to present the relationship between etching time and intensity, a series of graphs for each element keep a same range of intensity scale. (**d**) Decomposed O 1s spectra. Note that the C 1s (285 eV) used to calibrate the peak position.

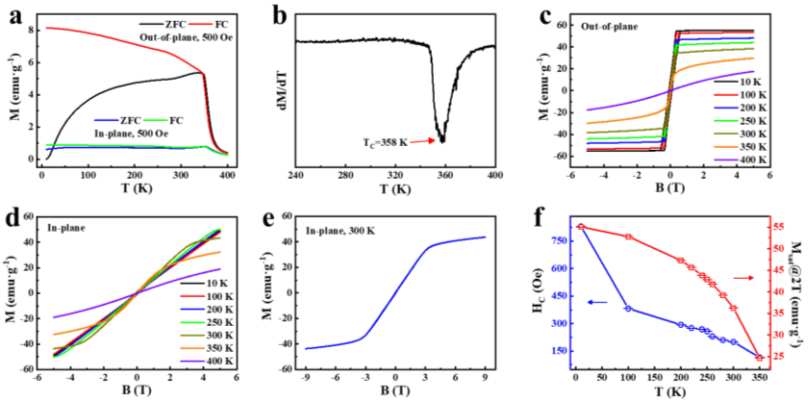

Figure S5. Above-room-temperature strong ferromagnetism in pristine vdW bulk Fe_3GaTe_{2-x} crystals. (**a**) Temperature-dependent ZFC-FC curves (M-T) under out-of-plane and in-plane magnetic field. (**b**) First derivative of the out-of-plane ZFC curve. The red arrow shows the ferromagnetic-paramagnetic transition. (**c,d**) M-B curves under varying temperatures with out-of-plane and in-plane magnetic field. (**e**) Room-temperature M-B curve for bulk Fe_3GaTe_{2-x} crystals with in-plane magnetic field from -9 to 9 T. The saturated field B_{sat} is ~3.5 T. (**f**) Temperature-dependent H_C and M_{sat} extracted from (**c**). Error bars sd., N=200.

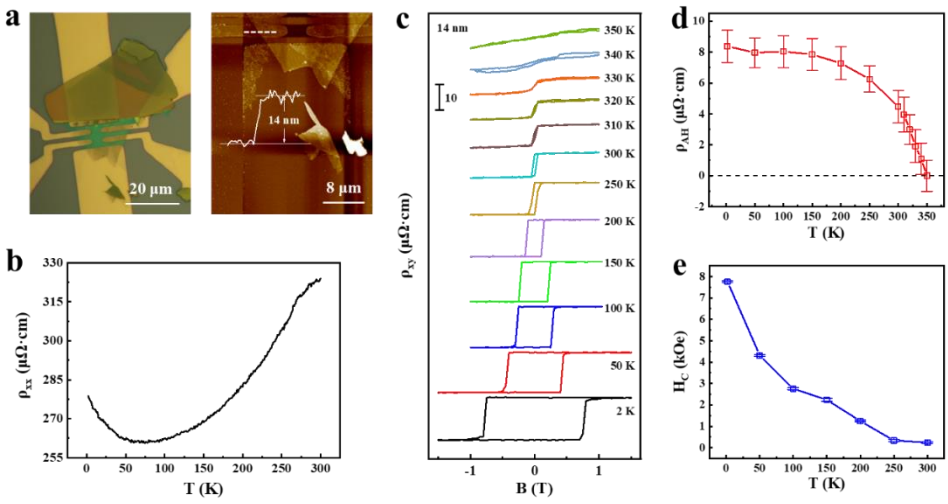

Figure S6. Magneto-transport measurement of a non-oxidized pristine 14 nm Fe_3GaTe_{2-x} nanosheet. (**a**) Optical and AFM images of a Hall device based on a Fe_3GaTe_{2-x} nanosheet. (**b**) Temperature-dependent longitudinal resistivity (ρ_{xx}) curve. The room temperature ρ_{xx} of this 14 nm nanosheet is 3.24×10^2 μΩ·cm. (**c**) AHE under different temperatures. The T_C is determined as ~350 K. (**d,e**) Temperature-dependent ρ_{AH} and H_C extracted from (**c**). Error bars sd., N=25 for ρ_{AH} and N=3 for H_C.

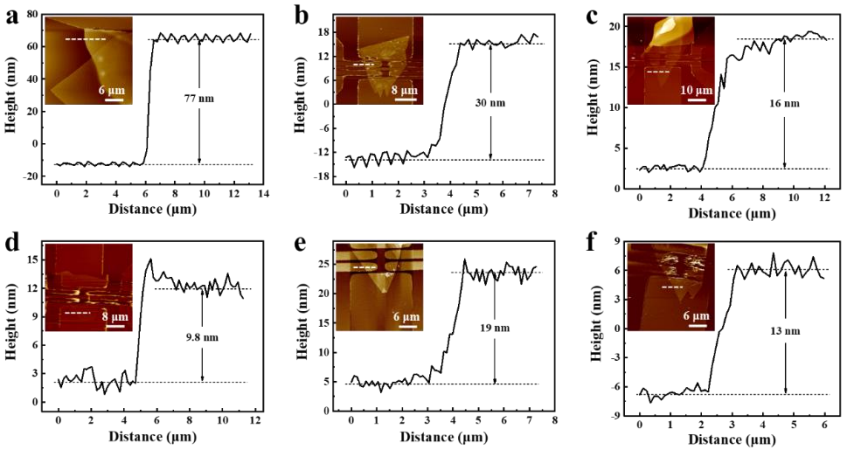

Figure S7. AFM images and the corresponded profile height of six as-tested Hall devices based on 2D O-FGaT/FGaT heterostructures.

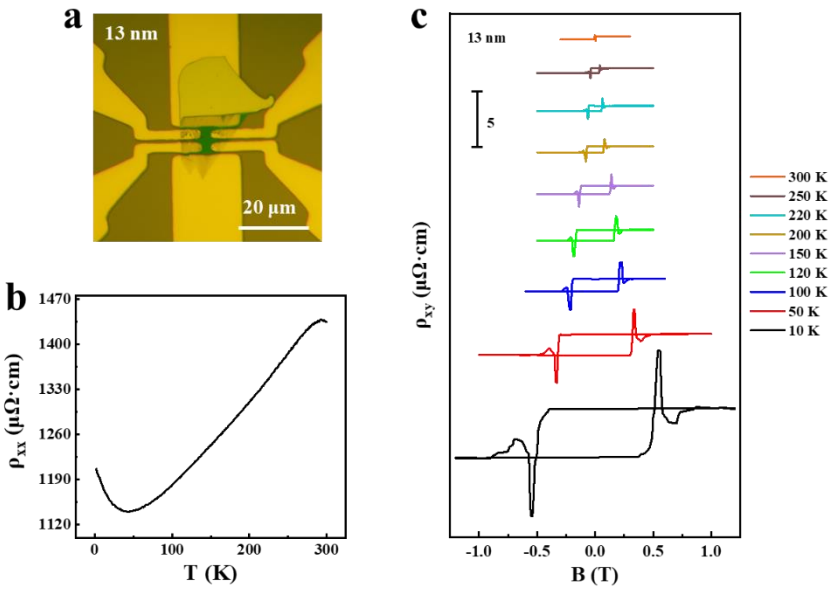

Figure S8. Magneto-transport measurement of a 13 nm 2D O-FGaT/FGaT heterostructure. (**a**) Optical image of the Hall device. (**b**) ρ_{xx}-T curve. Note that the 2D O-FGaT/FGaT still exhibits metallic nature. This is because oxidation occurs mainly on the upper surface of the sample exposed to air rather than the lower surface in contact with the electrodes. (**c**) ρ_{xy}-B curves at varying temperatures.

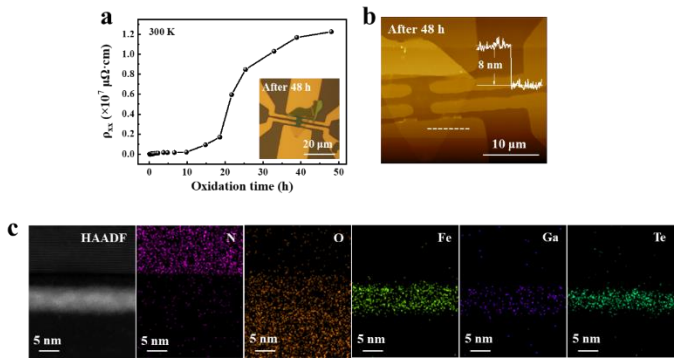

Figure S9. Natural total oxidation of the 2D Fe_3GaTe_{2-x} nanosheets in the air for 48 h. (**a**) ρ_{xx} as a function of oxidation time in the air. Inset shows the optical image of a Fe_3GaTe_{2-x} nanosheet after 48 h air oxidation. (**b**) Corresponded AFM image and profile height along the dash line. After the 48 h air oxidation, the thickness of this Fe_3GaTe_{2-x} nanosheet is 8 nm. (**c**) Cross-Sectional HAADF image and corresponded EDS elemental mapping of the 2D Fe_3GaTe_{2-x} nanosheet. The 48 h air oxidation is enough for totally oxidizing the Fe_3GaTe_{2-x} nanosheet, forming a ~8 nm O-FGaT layer.

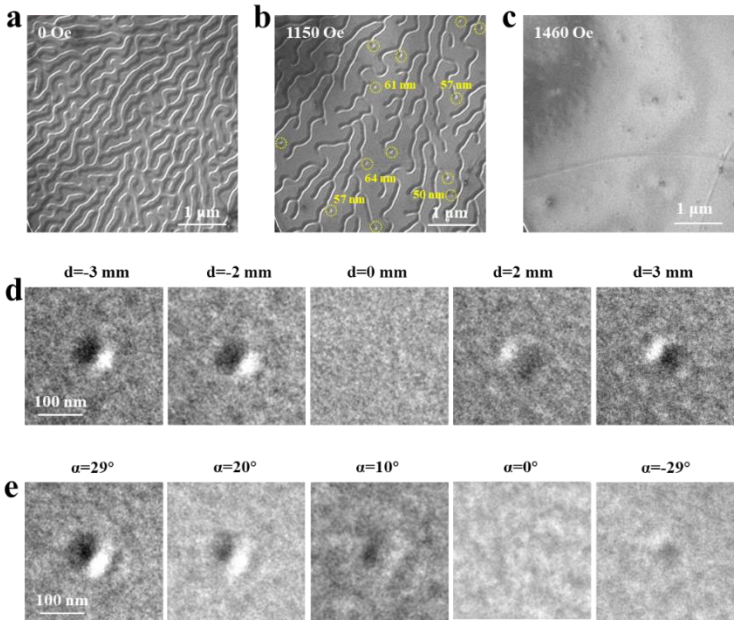

Figure S10. Observation of Néel-type skyrmions in 2D O-FGaT/FGaT by Lorentz-TEM with the perpendicular magnetic field at 300 K. (**a-c**) Magnetic-field-driven evolution from stripe domains to skyrmions at α=29°, d=-3 mm, where α is the angle between the sample plane and xy plane, d is the focus distance which positive represents the over-focus and negative represents the under-focus. (**d**) Single skyrmion under different d from under-focus to over-focus at α=29°, B=1400 Oe. (**e**) Single skyrmion under different α from 29° to -29 °at B=1360 Oe, d=-3 mm.

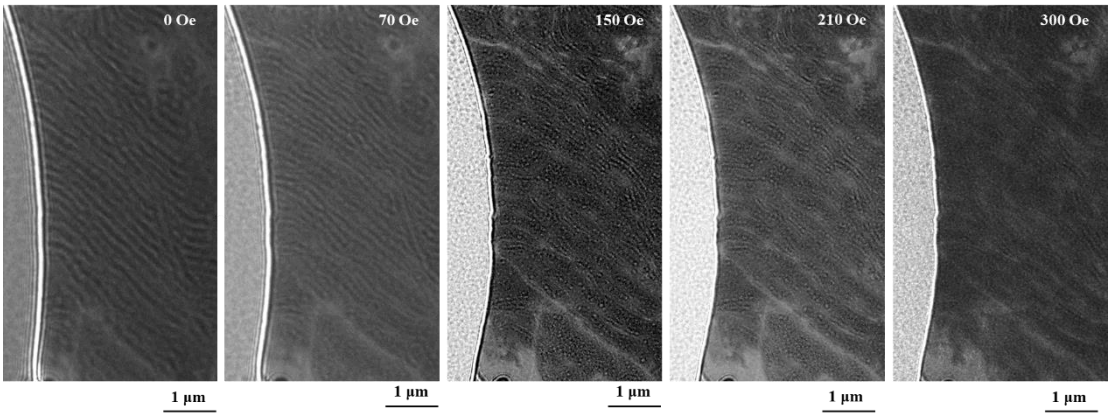

Figure S11. Magnetic-field-driven evolution from stripe domains to skyrmions in a thin 2D O-FGaT/FGaT by Lorentz-TEM with perpendicular magnetic field at 300 K. The images are taken at α=19° and d=-2 mm. At 150 Oe, the average skyrmion size calculated from 10 randomly-selected skyrmions is ~65 nm. The magnetic fields perpendicular to the sample are calculated as 0, 66, 142, 198 and 284 Oe.

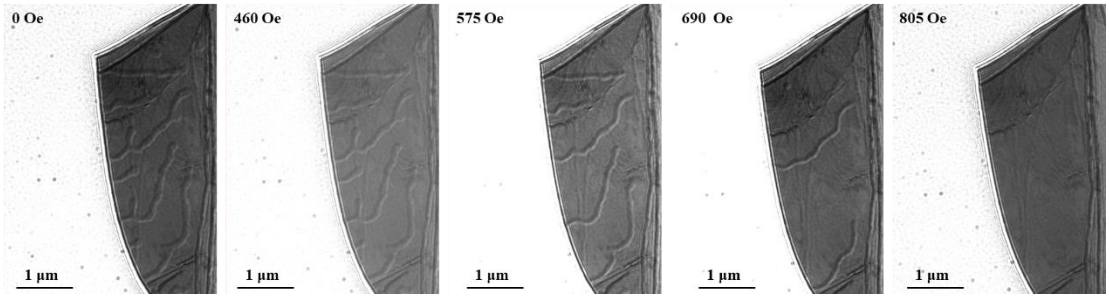

Figure S12. Lorentz-TEM images under different perpendicular magnetic field in a pristine non-oxidized thin 2D Fe_3GaTe_{2-x} nanosheet at 300 K under α=29°, d=-2 mm.

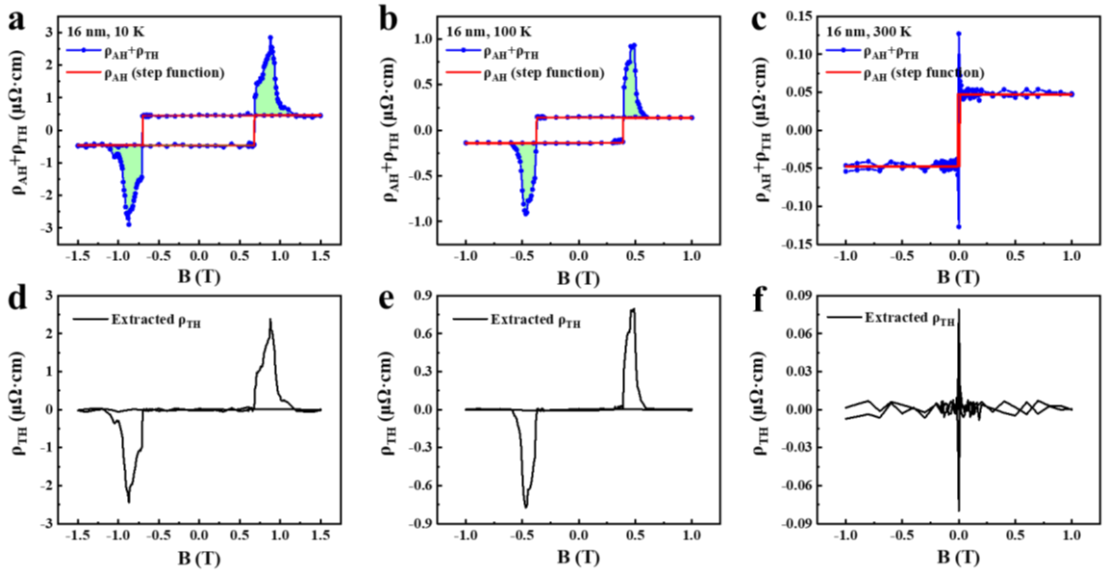

Figure S13. Extracting the THE signals in 2D O-FGaT/FGaT by step function. (**a-c**) ($\rho_{AH}+\rho_{TH}$) vs B curves at different temperatures. Contributions from AHE and THE terms are marked by red solid lines and light green area, respectively. (**d-f**) Corresponded ρ_{TH} vs B curves extracted from **a-c**.

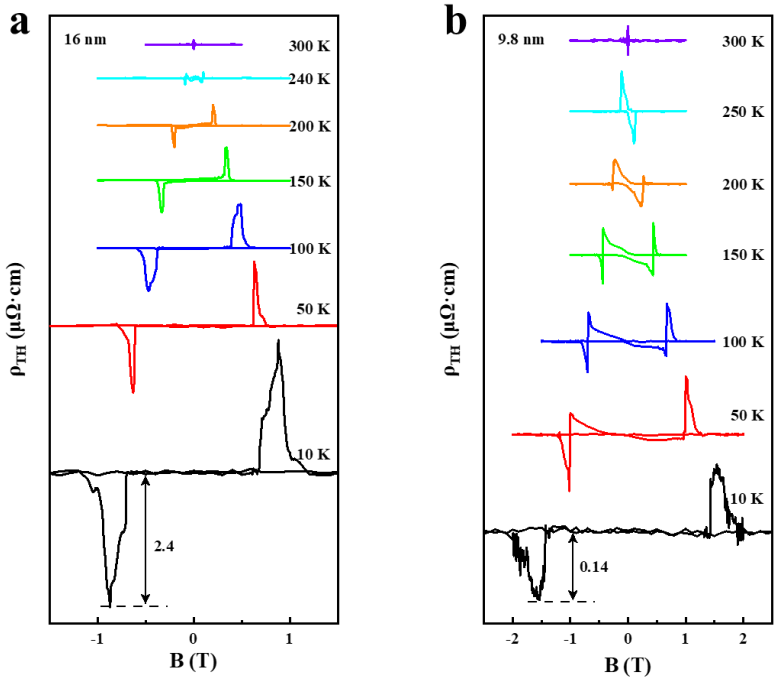

Figure S14. Temperature-dependent ρ_{TH}-B curves for two 2D O-FGaT/FGaT heterostructures with different thickness. (**a**) 16 nm. (**b**) 9.8 nm.

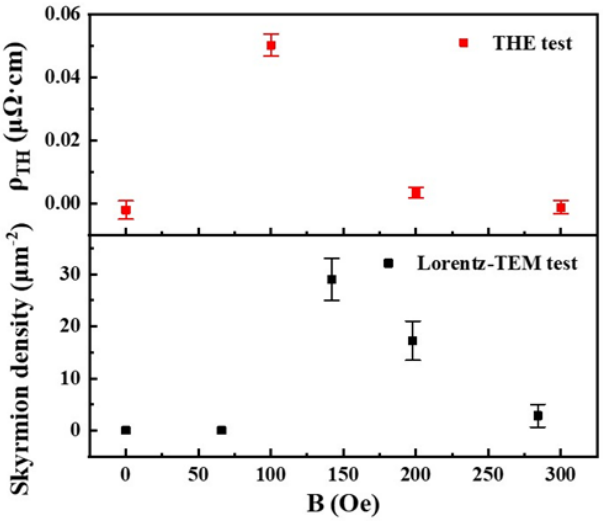

Figure S15. Magnetic field dependence of the skyrmion density and ρ_{TH} at room temperature in 2D O-FGaT/FGaT. The skyrmion density in each magnetic field is extracted from three randomly-selected 2 μm×2 μm regions in **Figure S11**. Error bars sd., N=3. The ρ_{TH} in each magnetic field is extracted from the 19 nm O-FGaT/FGaT in **main text Figure 3e**. Error bars sd., N=25. Note that the samples used here for THE test and Lorentz-TEM test are not the same sample.

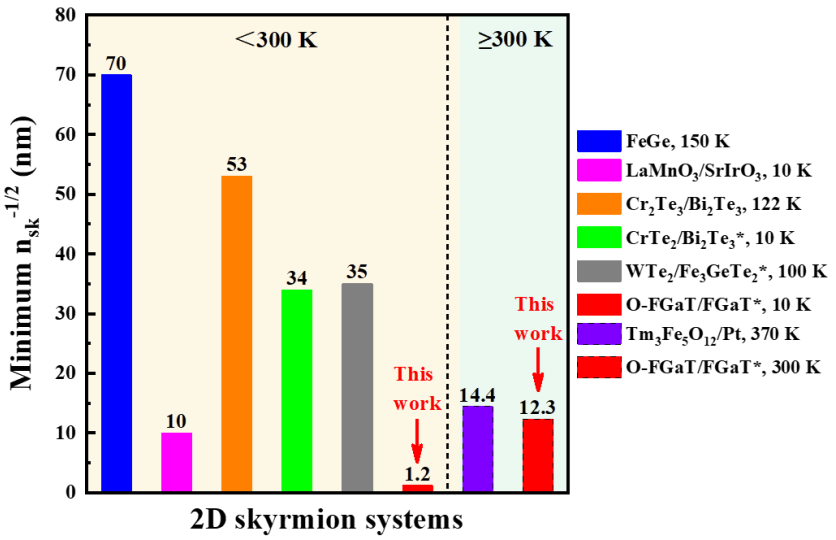

Figure S16. Comparison of THE tests-derived minimum skyrmion size ($n_{sk}^{-1/2}$) in various 2D skyrmion systems[19,23-27]**.** The [*] is the 2D vdW ferromagnet-based skyrmion systems.

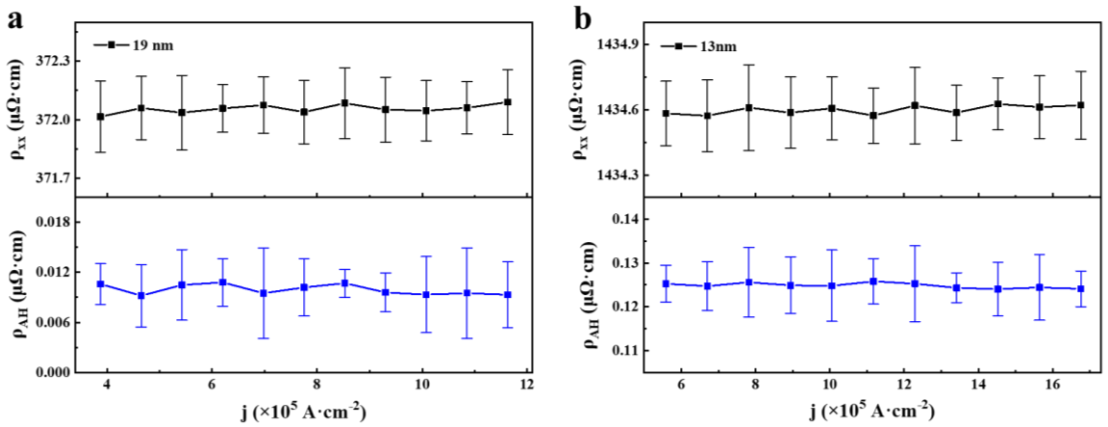

Figure S17. ρ_{xx} and saturated ρ_{AH} as a function of current densities in 2D O-FGaT/FGaT at room temperature. (**a**) 19 nm. (**b**) 13 nm. Error bars sd., N=25.

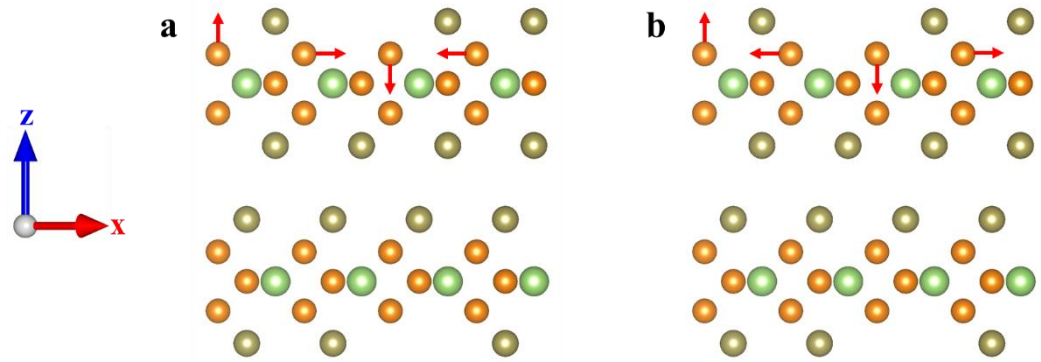

Figure S18. Theoretical model for calculating DMI in Fe_3GaTe_{2-x}. (**a,b**) Clockwise (CW) (**a**) and anticlockwise (ACW) (**b**) spin configurations of a bilayer Fe_3GaTe_{2-x} for calculating the layer-resolved d^L DMI parameters. The CW (ACW) spin configurations of a single layer Fe atoms are schematically shown by arrows. The spin of other Fe atoms points along the y-axis direction. The orange, green, brown balls denote Fe, Ga, Te atoms, respectively.

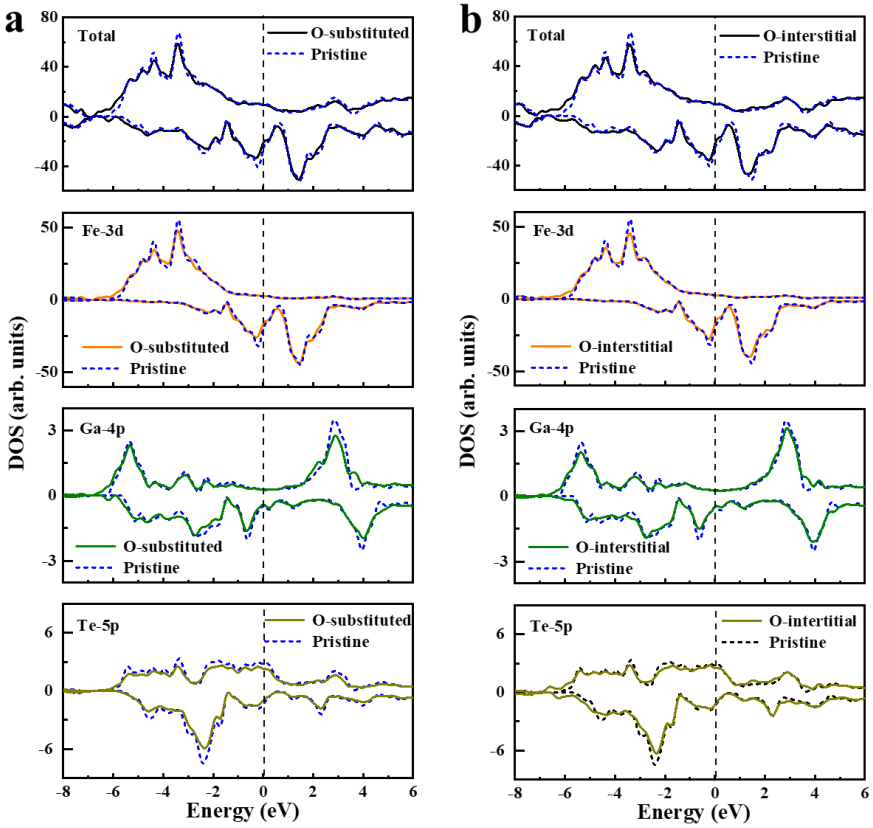

Figure S19. The density of states (DOSs) comparison of total, Fe-3d, Ga-4p, and Te-5p in oxidized bilayer Fe_3GaTe_{2-x} with that of pristine bilayer Fe_3GaTe_{2-x}. (**a**) O-substituted. (**b**) O-interstitial. The vertical dash lines denote the position of Fermi level. Note that DOSs of total, Fe-3d, Ga-4p, Te-5p all show the shift toward the low-energy direction after introducing surface oxygen atoms in two cases.

Table S1. Magneto-transport parameters for THE calculation in 2D O-FGaT/FGaT heterostructures with different thickness.

Thickness (nm)	T (K)	ρ_{TH} (μΩ·cm)	R_0 (Ω·m·T^{-1})	n (cm^{-3})	$n_{sk}^{-1/2}$ (nm)
19	2	1.08	1.05×10^{-11}	5.94×10^{23}	1.6
	300	0.05	7.95×10^{-11}	7.85×10^{22}	19
16	10	2.4	1.56×10^{-11}	4×10^{23}	1.4
	300	0.08	8.53×10^{-11}	7.32×10^{22}	15.6
13	10	5.4	2.72×10^{-11}	2.29×10^{23}	1.2
	300	0.15	9.97×10^{-11}	6.26×10^{22}	12.3

9.8	10	0.14	3.65×10^{-11}	1.71×10^{23}	8.5
	300	0.03	1.31×10^{-10}	4.76×10^{22}	31.5

Note: ρ_{TH} is the THE resistivity, R_0 is the ordinary Hall coefficient, n is the carrier concentration, $n_{sk}^{-1/2}$ is the THE tests-derived skyrmion size.

Table S2. Comparison of the THE temperature window and maximum ρ_{TH} in various 2D skyrmion systems from the literatures.

Materials	Temperature window (K)	Maximum ρ_{TH} (μΩ·cm)	Conditions for maximum ρ_{TH}	Ref.
FeGe	10-250	0.16	18 nm, 150 K	[23]
MnSi	2-50	0.025	20 nm, 40 K	[28]
Mn_2RhSn	15-200	0.26	60 nm, 140 K	[29]
Cr_2Te_3/Bi_2Te_3	2-95	0.4	5.5/19.8 nm, 122 K	[25]
Cr_2Te_3/Cr_2Se_3	10-75	0.25	10/20 nm, 10 K	[17]
$Bi_2Se_3/BaFe_{12}O_{19}$	2-80	0.23	6/5 nm, 2 K	[30]
$LaMnO_3/SrIrO_3$	3-50	75	5/5 u.c., 10 K	[24]
$Tm_3Fe_5O_{12}/Pt$	350-410	0.0046	4/3.2 nm, 370 K	[26]
$[Ir/Fe/Co/Pt]_{20}$	-	0.03	1/0.2/0.6/1 nm, 300 K	[31]
$[Co/Pt]_5$	-	0.01	0.5/1 nm, 300 K	[32]
Pt/Cr_2O_3	-	0.00065	2/3 nm, 300 K	[33]
$Cr_2Ge_2Te_6/Fe_3GeTe_2$*	2-100	0.31	30-40/4 nm, 2 K	[34]
$CrTe_2/Bi_2Te_3$*	10-100	1.39	6/- nm, 10 K	[19]
WTe_2/Fe_3GeTe_2*	2-100	1.3	3.2/1.1 nm, 2 K	[27]
$Sb_2Te_3/Sb_{1.9}V_{0.1}Te_3$*	6-40	0.48	3/5 QLs, 22 K	[35]
O-FGaT/FGaT*	**2-300**	**5.4**	**13 nm, 10 K**	**This**
		0.15	**13 nm, 300 K**	**work**

Note: [*] is the 2D vdW ferromagnet-based skyrmion systems.

Table S3. Comparison of critical current density (j_c) and maximum drift velocity (v_d) in various room-temperature 2D skyrmion systems from literatures.

Materials	Thickness (nm)	j_c (A·cm^{-2})	Maximum v_d (m·s^{-1})	Ref.
$[Pt/Co/Ta]_{15}$	3/0.9/4	2×10^7	50	[36]
$Ta/Co/[Pt/Ir/Co]_{10}/Pt$	15/0.8/1/1/0.8/3	2.7×10^7	20	[37]
Ta/Pt/Co/MgO/Ta	3/3/0.97/0.9/2	1.3×10^6	110	[38]
Pt/CoGd/Ta	6/5/3	7.5×10^7	500	[39]
Pt/CoGd/W	6/5/3	8×10^7	610	[39]
$[Pt/GdFeCo/MgO]_{20}$	3/5/1	1×10^7	50	[40]
$Ta/CoFeB/TaO_x$	5/1.2/5	1.39×10^6	0.45	[41]
$[Pt/CoFeB/MgO]_{15}$	4.5/0.7/1.4	2×10^7	100	[36]
O-FGaT/FGaT*	**13**	**7.82×10^5**	**0.82**	**This**
	19	**6.2×10^5**	**0.54**	**work**

Note: [*] is the 2D vdW ferromagnet-based skyrmion systems. The v_d in this Table is taken from the maximum value in each literature.

Table S4. The binding energies (E_b) for incorporating oxygen into Fe_3GaTe_{2-x} and Fe_3GaTe_2 crystals.

	O_2	Fe_3GaTe_2	O/Fe_3GaTe_2	$Fe_3GaTe_{1.7}$	$O/Fe_3GaTe_{1.7}$
E_b (eV)	-9.857	-139.486	-149.151	-134.285	-146.025

Note: for Fe_3GaTe_2: $E_1=E_{O/Fe_3GaTe_2}-E_{Fe_3GaTe_2}-\frac{1}{2}E_{O_2}$=-4.7365 eV

for $Fe_3GaTe_{1.7}$: $E_2=E_{O/Fe_3GaTe_{1.7}}-E_{Fe_3GaTe_{1.7}}-\frac{1}{2}E_{O_2}$=-6.8115 eV

Table S5. Average Bader charges (Q) of single atom in pristine, O-substituted, and O-interstitial bilayer Fe_3GaTe_{2-x}. The positive and negative Q values mean that the charges are transferred out of the atoms and transferred into the atoms, respectively.

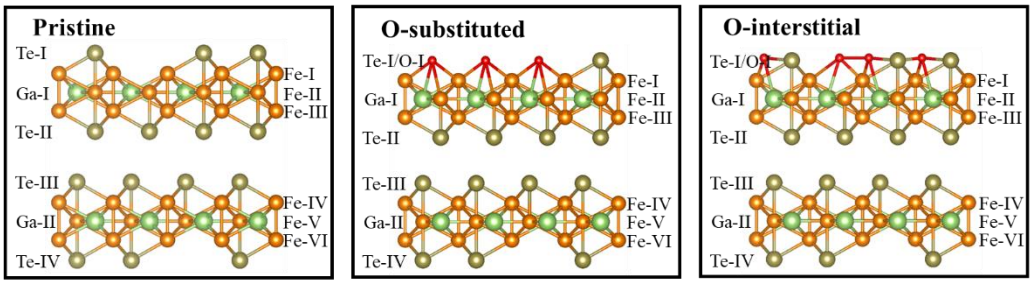

		Pristine	O-substituted	O-interstitial
Average Q (e) of single atom in each atomic layer of each case	Fe-I	0.23	**0.60**	**0.49**
	Fe-II	-0.15	**0.02**	**-0.09**
	Fe-III	0.24	0.21	0.22
	Fe-IV	0.23	0.25	0.25
	Fe-V	-0.15	-0.14	-0.17
	Fe-VI	0.24	0.22	0.22
	Ga-I	0.15	**0.28**	**0.23**
	Ga-II	0.15	0.13	0.16
	Te-I	-0.28	**-0.36**	**0.58**
	Te-II	-0.25	-0.25	-0.26
	Te-III	-0.25	-0.25	-0.25
	Te-IV	-0.28	-0.28	-0.28
	O-I	-	**-1.03**	**-1.02**
Average Q (e) of single atom in each case	Fe	0.11	**0.19**	**0.15**
	Ga	0.15	**0.21**	**0.19**
	Te	-0.26	-0.27	**-0.08**
	O	-	**-1.03**	**-1.02**

Note: The data marked in bold show that the average Q of single atom has significantly changed after introducing O atoms compared with that of pristine case. For the upper panel of this table, the Fe-I, Fe-II, etc. represent the atomic layers shown in upper images. After the introduction of O atoms,

the change of average Q mainly happens in the atomic layers adjacent to O atoms, such as Fe-I, Fe-II, Ga-I and Te-I. For the lower panel of this table, after the introduction of O atoms, the increase of average Q for Fe and Ga atoms and the decrease of average Q for Te atoms all indicate that part of charge is transferred from these atoms to O atoms.

Supporting References

[1] Kaihang Ye, Kunshan Li, Yirui Lu, Zhongjie Guo, Nan Ni, Hong Liu, Yongchao Huang, Hongbing Ji, and P. Wang 2019 *Trends Anal. Chem.* **116** 102

[2] E. Paparazzo, G. M. Ingo, and N. Zacchetti 1991 *J. Vac. Sci. Technol. A* **9** 1416

[3] F. Y. Xie, L. Gong, X. Liu, Y. T. Tao, W. H. Zhang, S. H. Chen, H. Meng, and J. Chen 2012 *J. Electron. Spectrosc.* **185** 112

[4] Z. Fei, B. Huang, P. Malinowski, W. Wang, T. Song, J. Sanchez, W. Yao, D. Xiao, X. Zhu, A. F. May, W. Wu, D. H. Cobden, J. H. Chu, and X. Xu 2018 *Nat. Mater.* **17** 778

[5] C. Gong, L. Li, Z. Li, H. Ji, A. Stern, Y. Xia, T. Cao, W. Bao, C. Wang, Y. Wang, Z. Q. Qiu, R. J. Cava, S. G. Louie, J. Xia, and X. Zhang 2017 *Nature* **546** 265

[6] B. Huang, G. Clark, E. Navarro-Moratalla, D. R. Klein, R. Cheng, K. L. Seyler, D. Zhong, E. Schmidgall, M. A. McGuire, D. H. Cobden, W. Yao, D. Xiao, P. Jarillo-Herrero, and X. Xu 2017 *Nature* **546** 270

[7] M. Huang, S. Wang, Z. Wang, P. Liu, J. Xiang, C. Feng, X. Wang, Z. Zhang, Z. Wen, H. Xu, G. Yu, Y. Lu, W. Zhao, S. A. Yang, D. Hou, and B. Xiang 2021 *ACS Nano* **15** 9759

[8] S. Ikeda, K. Miura, H. Yamamoto, K. Mizunuma, H. D. Gan, M. Endo, S. Kanai, J. Hayakawa, F. Matsukura, and H. Ohno 2010 *Nat. Mater.* **9** 721

[9] G. Zhang, F. Guo, H. Wu, X. Wen, L. Yang, W. Jin, W. Zhang, and H. Chang 2022 *Nat. Commun.* **13** 5067

[10] X. Zhang, Q. Lu, W. Liu, W. Niu, J. Sun, J. Cook, M. Vaninger, P. F. Miceli, D. J. Singh, S. W. Lian, T. R. Chang, X. He, J. Du, L. He, R. Zhang, G. Bian, and Y. Xu 2021 *Nat. Commun.* **12** 2492

[11] G. Kimbell, P. M. Sass, B. Woltjes, E. K. Ko, T. W. Noh, W. Wu, and J. W. A. Robinson 2020 *Phys. Rev. Mater.* **4** 054414

[12] K. M. Fijalkowski, M. Hartl, M. Winnerlein, P. Mandal, S. Schreyeck, K. Brunner, C. Gould, and L. W. Molenkamp 2020 *Phys. Rev. X* **10** 011012

[13] A. Gerber 2018 *Phys. Rev. B* **98** 214440

[14] D. Kan, T. Moriyama, K. Kobayashi, and Y. Shimakawa 2018 *Phys. Rev. B* **98** 180408(R)

[15] L. Wang, Q. Feng, H. G. Lee, E. K. Ko, Q. Lu, and T. W. Noh 2020 *Nano Lett.* **20** 2468

[16] G. Kimbell, C. Kim, W. Wu, M. Cuoco, and J. W. A. Robinson 2022 *Commun Mater* **3** 19

[17] J. H. Jeon, H. R. Na, H. Kim, S. Lee, S. Song, J. Kim, S. Park, J. Kim, H. Noh, G. Kim, S. K. Jerng, and S. H. Chun 2022 *ACS Nano* **16** 8974

[18] L. Tai, B. Dai, J. Li, H. Huang, S. K. Chong, K. L. Wong, H. Zhang, P. Zhang, P. Deng, C. Eckberg, G. Qiu, H. He, D. Wu, S. Xu, A. Davydov, R. Wu, and K. L. Wang 2022 *ACS Nano* **16** 17336

[19] X. Zhang, S. C. Ambhire, Q. Lu, W. Niu, J. Cook, J. S. Jiang, D. Hong, L. Alahmed, L. He, R. Zhang, Y. Xu, S. S. Zhang, P. Li, and G. Bian 2021 *ACS Nano* **15** 15710

[20] W. Zhu, S. Xie, H. Lin, G. Zhang, H. Wu, T. Hu, Z. Wang, X. Zhang, J. Xu, Y. Wang, Y. Zheng, F. Yan, J. Zhang, L. Zhao, A. Patanè, J. Zhang, H. Chang, and K. Wang 2022 *Chin. Phys. Lett.* **39** 128501
[21] Hongrui Zhang, David Raftrey, Ying-Ting Chan, Yu-Tsun Shao, Rui Chen, Xiang Chen, Xiaoxi Huang, Jonathan T. Reichanadter, Kaichen Dong, Sandhya Susarla, Lucas Caretta, Zhen Chen, Jie Yao, Peter Fischer, Jeffrey B. Neaton, Weida Wu, David A. Muller, Robert J. Birgeneau, and R. Ramesh 2022 *Sci. Adv.* **8** eabm7103
[22] D. Liang, J. P. DeGrave, M. J. Stolt, Y. Tokura, and S. Jin 2015 *Nat. Commun.* **6** 8217
[23] S. X. Huang and C. L. Chien 2012 *Phys. Rev. Lett.* **108** 267201
[24] Elizabeth Skoropata, John Nichols, Jong Mok Ok, Rajesh V. Chopdekar, Eun Sang Choi, Ankur Rastogi, Changhee Sohn, Xiang Gao, Sangmoon Yoon, Thomas Farmer, Ryan D. Desautels, Yongseong Choi, Daniel Haskel, John W. Freeland, Satoshi Okamoto, Matthew Brahlek, and H. N. Lee 2020 *Sci. Adv.* **6** eaaz3902
[25] J. Chen, L. Zhou, L. Wang, Z. Yan, X. Deng, J. Zhou, J.-w. Mei, Y. Qiu, B. Xi, X. Wang, H. He, and G. Wang 2021 *Cryst. Growth. Des.* **22** 140
[26] Q. Shao, Y. Liu, G. Yu, S. K. Kim, X. Che, C. Tang, Q. L. He, Y. Tserkovnyak, J. Shi, and K. L. Wang 2019 *Nat. Electron.* **2** 182
[27] Y. Wu, S. Zhang, J. Zhang, W. Wang, Y. L. Zhu, J. Hu, G. Yin, K. Wong, C. Fang, C. Wan, X. Han, Q. Shao, T. Taniguchi, K. Watanabe, J. Zang, Z. Mao, X. Zhang, and K. L. Wang 2020 *Nat. Commun.* **11** 3860
[28] T. Yokouchi, N. Kanazawa, A. Tsukazaki, Y. Kozuka, M. Kawasaki, M. Ichikawa, F. Kagawa, and Y. Tokura 2014 *Phys. Rev. B* **89** 064416
[29] P. K. Sivakumar, B. Gobel, E. Lesne, A. Markou, J. Gidugu, J. M. Taylor, H. Deniz, J. Jena, C. Felser, I. Mertig, and S. S. P. Parkin 2020 *ACS Nano* **14** 13463
[30] P. Li, J. Ding, S. S. Zhang, J. Kally, T. Pillsbury, O. G. Heinonen, G. Rimal, C. Bi, A. DeMann, S. B. Field, W. Wang, J. Tang, J. S. Jiang, A. Hoffmann, N. Samarth, and M. Wu 2021 *Nano Lett.* **21** 84
[31] A. Soumyanarayanan, M. Raju, A. L. Gonzalez Oyarce, A. K. C. Tan, M. Y. Im, A. P. Petrovic, P. Ho, K. H. Khoo, M. Tran, C. K. Gan, F. Ernult, and C. Panagopoulos 2017 *Nat. Mater.* **16** 898
[32] M. V. Sapozhnikov, N. S. Gusev, S. A. Gusev, D. A. Tatarskiy, Y. V. Petrov, A. G. Temiryazev, and A. A. Fraerman 2021 *Phys. Rev. B* **103** 054429
[33] Y. Cheng, S. Yu, M. Zhu, J. Hwang, and F. Yang 2019 *Phys. Rev. Lett.* **123** 237206
[34] Y. Wu, B. Francisco, Z. Chen, W. Wang, Y. Zhang, C. Wan, X. Han, H. Chi, Y. Hou, A. Lodesani, G. Yin, K. Liu, Y. T. Cui, K. L. Wang, and J. S. Moodera 2022 *Adv. Mater.* **34** e2110583
[35] W. Wang, Y. F. Zhao, F. Wang, M. W. Daniels, C. Z. Chang, J. Zang, D. Xiao, and W. Wu 2021 *Nano Lett.* **21** 1108
[36] S. Woo, K. Litzius, B. Kruger, M. Y. Im, L. Caretta, K. Richter, M. Mann, A. Krone, R. M. Reeve, M. Weigand, P. Agrawal, I. Lemesh, M. A. Mawass, P. Fischer, M. Klaui, and G. S. Beach 2016 *Nat. Mater.* **15** 501
[37] W. Legrand, D. Maccariello, N. Reyren, K. Garcia, C. Moutafis, C. Moreau-Luchaire, S. Collin, K. Bouzehouane, V. Cros, and A. Fert 2017 *Nano Lett.* **17** 2703
[38] R. Juge, K. Bairagi, K. G. Rana, J. Vogel, M. Sall, D. Mailly, V. T. Pham, Q. Zhang, N. Sisodia, M. Foerster, L. Aballe, M. Belmeguenai, Y. Roussigne, S. Auffret, L. D. Buda-Prejbeanu, G. Gaudin, D. Ravelosona, and O. Boulle 2021 *Nano Lett.* **21** 2989

[39] Y. Quessab, J. W. Xu, E. Cogulu, S. Finizio, J. Raabe, and A. D. Kent 2022 *Nano Lett.* **22** 6091
[40] S. Woo, K. M. Song, X. Zhang, Y. Zhou, M. Ezawa, X. Liu, S. Finizio, J. Raabe, N. J. Lee, S. I. Kim, S. Y. Park, Y. Kim, J. Y. Kim, D. Lee, O. Lee, J. W. Choi, B. C. Min, H. C. Koo, and J. Chang 2018 *Nat. Commun.* **9** 959
[41] G. Yu, P. Upadhyaya, Q. Shao, H. Wu, G. Yin, X. Li, C. He, W. Jiang, X. Han, P. K. Amiri, and K. L. Wang 2017 *Nano Lett.* **17** 261